Nationaal Lucht- en Ruimtevaartlaboratorium
National Aerospace Laboratory NLR

NLR-TP-2003-397

Towards the simulation of unsteady manoeuvre dominated by vortical flow

Common Exercise I of WEAG THALES JP12.15

B.I. Soemarwoto, O.J. Boelens, M. Allan, M.T. Arthur,
K. Bütefisch, N. Ceresola and W. Fritz

Nationaal Lucht- en Ruimtevaartlaboratorium
National Aerospace Laboratory NLR

NLR-TP-2003-397

Towards the simulation of unsteady manoeuvre dominated by vortical flow

Common Exercise I of WEAG THALES JP12.15

B.I. Soemarwoto, O.J. Boelens, M. Allan[1], M.T. Arthur[2],
K. Bütefisch[3], N. Ceresola[4] and W. Fritz[5]

1 University of Glasgow, United Kingdom
2 QinetiQ, United Kingdom
3 German Aerospace Center DLR, Germany
4 Alenia Aeronautica, Italy
5 EADS, Germany

This report is based on a presentation held at the 21st Applied Aerodynamics Conference, Orlando (FL), U.S.A., 23-26 June 2003.
The Ministry of Defence has granted NLR permission to publish this report.

Customer:	Ministry of Defence
Working Plan number:	1.1.H.2c/A.1.A.2
Owner:	National Aerospace Laboratory NLR
Division:	Fluid Dynamics
Distribution:	Unlimited
Classification title:	Unclassified
	August 2003

Approved by author:	Approved by project manager:	Approved by project managing department:
8/9	8/9	9/9/2003

Summary

The paper addresses the applicability of unsteady Reynolds-Averaged Navier-Stokes CFD methods for the simulation of transonic vortical flow around delta wings. Three transonic flow cases are considered: a static delta wing, a delta wing rolling with a constant rate around the body axis, and a delta wing rolling with a constant rotational rate around the wind axis. Comparison of the computational results with experimental data, and comparison of results obtained using different CFD codes, are presented in terms of the flow quantities such as pressure coefficient, skin-friction, total pressure loss and turbulence intensities, and in terms of the flow phenomena such as vortex breakdown and primary and secondary leading edge vortices. The differences in the flow solutions are discussed in relation with the discretisation schemes and the turbulence models used in the different codes.

The results presented are an outcome of the research conducted by Alenia (Italy), EADS (Germany), NLR (The Netherlands), University of Glasgow and QinetiQ (United Kingdom) for the numerical work, and DLR (Germany) for the experimental work, which has been performed within Common Exercise I under the framework of European programme WEAG Thales JP12.15.

Contents

22 Figures

(35 pages in total)

Nomenclature

b	wing span
C_L	lift coefficient
C_D	drag coefficient
C_M	pitching moment coefficient
C_l	rolling moment coefficient
C_p	pressure coefficient
M_∞	free-stream Mach number
p_t	total pressure
C_f	skin friction coefficient, $C_f = \|\vec{\tau}_w\|/\frac{1}{2}\rho_\infty U_\infty^2$
c	wing root chord
m_i, φ_i	magnitude and phase of the i-th harmonics
n_0	physical roll-rate (rps), $n_0 = (\partial\phi/\partial t)/(2\pi)$
p	non-dimensional roll-rate, $p = 2\pi n_0 b/U_\infty$
U_∞	magnitude of the free-stream velocity
x, y, z	Cartesian coordinates of the body axis
$\mathbf{x}_m$	coordinates of the moment reference point
Re	Reynolds number based on c
α	angle of attack
α_0	maximum angle of attack in roll-motion
η	local non-dimensional spanwise coordinate
μ	dynamic molecular viscosity
μ_T	turbulence eddy viscosity
ρ_∞	free-stream density

$\vec{\tau}_w$	wall shear stress on the surface
ϖ	non-dimensional rotation-rate
	w.r.t. the wind axis,$\varpi = (\partial\Phi/\partial t)b/U_\infty$
Φ	rotation-angle w.r.t. the wind axis
ϕ	roll-angle w.r.t. the inertial axis

1 Introduction

In recent decades fighter aircraft design has been pushed towards the expansion of flight envelopes into extreme conditions and aggressive manoeuvres with high angles of attack and high angular rates, involving strongly unsteady vortical flow phenomena. The advent of high angle of attack control effectors, such as thrust vectoring and forebody control, adds to the complexity as the design is pushed even further into high angular rate regimes. These features of modern high performance aircraft potentially increase the air combat exchange ratio because of enhanced tactical agility. On the other hand, they can also result in extremely challenging stability and control problems, increasing the probability of departure from controlled flight, and therefore increasing the probability of mishap involving loss of aircraft and/or pilot. As the flight envelopes are being expanded, fighter aircraft programmes increasingly rely on simulation-based predictions to minimise the life-cycle cost. Accurate simulations are critical for sustainable cost reduction, because fixes based on post-accident analysis are expensive.

This paper addresses vortical flows around generic delta wings in transonic conditions with high angles of attack. The present investigation is part of a continuing collaborative research programme on the simulation of vortical flows, with the long term objective to enable the simulation of unsteady manoeuvres of military air vehicles using CFD methodology. The preceding investigations (Refs. 1-9) covered steady inviscid flow simulations, steady viscous flow simulations, and unsteady inviscid flow simulations. The conclusions drawn in the study of unsteady vortical flow around a delta wing in roll-motion by means of inviscid (Euler) time-accurate simulation methods (Refs. 8, 9) partly forms the basis of the present investigation with the objectives (i) to evaluate the applicability of unsteady RANS methods for the simulation of transonic vortical flows around delta wings by comparing computed results with experimental data and through code-to-code comparison, (ii) to investigate whether the unsteady RANS methods are able to explain the discrepancies previously observed (Ref. 9) , and (iii) to assess the feasibility of simulating realistic flight roll motions for a generic delta wing at transonic speed using unsteady RANS methods.

The paper is organized as follows. The next section presents the definition of the test cases involving two generic delta wings and three transonic flow conditions. Subsequently, the solution algorithms underlying four different CFD codes applied by Alenia (Italy), EADS-M (Germany), NLR (The Netherlands), and QinetiQ and University of Glasgow (United Kingdom) are described. After this section, a comparison and discussion of the computational and experimental results is given leading to conclusions.

2 Test Case Definition

Three test cases are considered using two delta wing models, the PSP and WI1-SLE model, having a planform shown in Figure 1. Case 1 and 2 concern the PSP model which consists of a sharp-edged delta wing and a fuselage starting at the wing apex (Figure 2). Case 3 concerns the WI1-SLE model which does not have a fuselage (Figure 3).

Case 1 represents a static delta wing in a transonic flow at a free-stream Mach number $M_\infty = 0.8$, an angle of attack $\alpha = 17^o$, and a Reynolds number Re $= 5.3 \times 10^6$. Case 2 is an unsteady flow test case where the delta wing makes a roll-motion about the body-axis at a non-dimensional constant rate $p = 0.0762$. The maximum angle of attack occurring in this roll-motion is $\alpha_0 = 17^o$. The Mach and Reynolds numbers are the same as those of Case 1. The direction of the roll-motion is counter-clockwise from the pilot-view (Figure 2). The zero roll-angle ($\phi = 0^o$) corresponds to the maximum angle of attack α_0 when the axis of the body coincides the inertial (earth-fixed) axis. The unsteady computation is performed for three full cycles with 72 steps per cycle, giving an increment of 5 degrees in the roll-angle.

Case 3 represents an unsteady flow test case for an isolated delta wing in roll-motion at a constant rotational rate, $\varpi = 0.08$, about the wind-axis at $M_\infty = 0.85$, $\alpha = 10^o$ and Re $= 9.0 \times 10^6$. This rotational rate corresponds to a roll-rate of about $300^o/s$, representative for a full-scale modern fighter aircraft configuration in a typical realistic manoeuvre. The rotation axis (parallel to the flight direction) intersects the body axis at the moment reference point at $\mathbf{x}_m = (0.5625, 0, 0)$. The roll-motion is counter-clockwise from the pilot-view (Figure 3). As the wind axis is used for the axis of rotation, the onset flow makes a constant angle of attack with the body axis. Accordingly, the flow can also be considered as steady in a rotating body frame of reference.

3 Solution Algorithms

The time-dependent Reynolds-Averaged Navier-Stokes (RANS) equations are employed. For the determination of the Reynolds stress tensor, variants of two-equation turbulence models are used. The turbulence equations and the mean flow (RANS) equations are solved simultaneously for the mean flow variables, the turbulence kinetic energy k, and the eddy viscosity μ_t. Four codes are applied for obtaining the flow solutions.

At Alenia, the solutions have been obtained by means of the code UNS3D, which is based on a finite volume scheme with node centred approach on an unstructured grid (Ref. 21) . The artificial dissipation model is derived from the nonlinear scheme of Jameson. Two-equation k-R_t wall distance free turbulence model is employed, with Favre averaging applied to account for compressibility effects. To limit the value of the production-to-dissipation ratio, the Menter's SST limiter is implemented. The equations for turbulence quantities are solved with the same technique as that used for the flow variables. An implicit treatment of the source terms is implemented. The Navier-Stokes equations are integrated in time with a second order backward difference. The ALE (Arbitrary Lagrangian Eulerian) description is adopted, so that the motion of the fluid is considered in a fixed frame of reference, while the grid is attached to the rotating model.

At EADS, the calculations have been performed using the FLOWer Code (Ref. 10) . This code has been developed in a national German collaboration under the direction of DLR, with essential contributions of other participants (among others, Airbus, DASA-M, Technical University of Berlin). The Jameson-type scheme is employed with a cell-vertex finite volume approach using spatial central differences in block-structured grids, combined with a Runge-Kutta scheme for the time integration towards steady-state. The standard Wilcox k-ω model (Ref. 11) with the original closure coefficients has been used in steady and unsteady calculations. The flow equations and the turbulent transport equations are solved synchronously within the time integration.

At the University of Glasgow, the mean flow RANS equations are discretised on curvilinear multi-block body conforming grids using a cell-centred finite volume method. The convective terms are discretised using Osher's upwind scheme (Ref. 16) . MUSCL variable extrapolation is used to provide second-order accuracy with the Van Albada limiter to prevent spurious oscillations around shock waves. An implicit time marching scheme is employed to solve the discretised equations. The Jacobian of the residual is approximated with first order accuracy (Ref. 17) to reduce the number of terms in the matrix per cell by a factor of 5. A Krylov subspace algorithm is used to solve the linear system of equations and is preconditioned using a Block Incomplete Lower-Upper factorisation with the same sparsity pattern as the Jacobian matrix (Ref. 18) . The k-ω turbulence

model of Wilcox (Ref. 11) is used and implemented using a numerical method similar to the one applied to the mean flow equations. The mean flow and turbulence equations are solved in sequence by the steady state solver (Ref. 20) .

At NLR, the mean flow (RANS) equations and the k-ω turbulence model are solved as one system of equations by means of the CFD system ENFLOW (Ref. 15) . The flow field is represented by a multi-block domain containing structured grids. For the mean flow equations, Jameson-type artificial dissipation fluxes are added in combination with matrix coefficients to enhance accuracies inside the boundary layers. A variant of the Wilcox k-ω turbulence model is employed, where an additional cross-diffusion term has been introduced to resolve the free-stream dependency of the solutions (Ref. 12) . Also, the τ formulation for ω is implemented to avoid the singular behaviour of ω near solid walls, where $\tau = 1/\omega$ is treated as a dependent variable (Ref. 13) instead of ω.

For time-accurate calculations, all codes apply Jameson's pseudo-time (dual-time stepping) formulation (Ref. 19) with the steady state solver used to calculate for the flow steady states on each physical time-step.

It is well-known that for vortical flows the standard Wilcox $k-\omega$ model is too diffusive to capture flow details near vortex cores. High turbulence kinetic energy induces excessively high eddy viscosities. In order to limit the extreme eddy viscosity production in the vortex core, modifications to the turbulence models have been applied.

At EADS, a uniform production limiter is introduced for the k-production. At NLR, a limiter sensitive to the vortex structure is introduced by means of a parameter r representing the ratio between the magnitude of the strain-rate tensor and the magnitude of the vorticity. In shear layers, the velocity gradient is dominated by the gradient in the normal direction, which gives $r \approx 1$. In vortex cores, $r \leq 1$ where the flow approaches pure rotation. This property is used to detect vortex cores and subsequently to control the production of eddy viscosity. There are two possible approaches (Ref. 14) : (i) to limit the production term in the k equation, and (ii) to increase the production term in the ω equation giving the effect of increasing the dissipation the turbulence kinetic energy and therefore the eddy viscosity. In the present exercise, NLR applied the second approach through increasing the production of ω, while the results of the University of Glasgow are obtained by directly limiting the production of k.

4 Results and discussion

4.1 Case 1: static delta wing

The experiment was performed in the Transonic Wind Tunnel (TWG) at DLR Göttingen. This tunnel is a continuously driven facility that operates at Mach numbers between 0.3 and 0.85 using a $1m \times 1m$ test section with adaptive walls. Figure 4 shows the model in the TWG and components of the DLR PSP system with cameras and illuminators attached to the wall (Refs. 22-24) .

Figure 5 shows the experimental surface pressure distribution for the steady case. A top-view of the delta wing configuration gives an impression of the fuselage and the wing-fuselage fairing. The blue-coloured corner region near the left wing tip and the trailing edge is a region where experimental data could not be recorded. Visible in both images are thin "lines" along the wing-fuselage fairing. These lines are by-products of the PSP data processing and should not be interpreted as physical.

A CO-topology is used for the computational grids (Figure 6). The grids feature a singular line running from the apex to the upstream far-field, and have O-type singularities at both sides running from the trailing edge to the downstream far-field boundaries. The grid dimension is $144 \times 320 \times 64$ giving a total number of grid cells of $2,949,120$.

Figure 7 shows the upper surface C_p contours obtained from the numerical solutions. The Alenia solution is obtained from a calculation for a half delta wing configuration, on a grid coarsened by taking every other point in the chordwise direction. This coarsening is considered not to have a large effect on the crossflow structure of the vortex, as the spanwise resolution remains the same. It should also be noted that in the University of Glasgow solution a small laminar region is imposed along the leading edges.

Along the centerline region up to about $x/c = 0.30$, all numerical results show a local minimum near the point where the fuselage has attained its maximum height. A contraction of the wing-fuselage fairing can be seen as implying a local positive pressure gradient, which has possibly led to a small region of flow separation.

Further downstream, the flows develop into two different families of pressure contours, distinguished by whether or not vortex breakdown has occurred in the solution. Without vortex breakdown (the solutions of EADS and Alenia), the pressure increases along the centerline quite monotonically towards its level at the trailing edge. With vortex breakdown, as in the solutions of University of Glasgow and NLR, there is a local maximum that appears to be confined in a region just upstream of the vortex breakdown. The PSP data shows no indication of vortex breakdown.

Distinct secondary vortices can already be seen in the University of Glasgow solution from locations near the apex. The Alenia solution shows a secondary vortex at $x/c \approx 0.15$, but upstream of this location the pattern of the pressure contours appears to be irregular. In the NLR solution, the secondary vortex is observed beginning at $x/c \approx 0.20$, but then it seems to be hampered by the effect of the wing-fuselage fairing contraction. A similar situation occurs with the EADS solution. The effect can also be observed in the University of Glasgow solution, where the secondary vortex appears to be inhibited locally at $x/c \approx 0.25$. Upstream this region, all numerical results show that the secondary vortices have fully developed.

The vortex breakdown occurs earlier ($\approx$ 70% of chord) in the University of Glasgow solution than in the NLR solution ($\approx$ 75% of chord). This situation can be attributed to the more compact vortex in the University of Glasgow solution, presumably due to the Osher's scheme which is known to be less dissipative than the central scheme with artificial dissipations employed in the NLR method.

Comparing the solutions without vortex breakdown, the primary vortex in the Alenia solution appears to be more compact than in the EADS solution. Contradictory to the common tendency that a more compact vortex is less stable, the Alenia solution indicates a more stable vortex, as it has largely maintained its structure up to near the trailing edge. This situation may be attributed to larger numerical dissipations associated with the coarser grid used in the Alenia solution.

Figure 8 shows the skin friction contours and the shear-stress streamline patterns. The separation line leading to the secondary vortex, and the corresponding attachment line, can be seen in both the University of Glasgow and NLR solutions. Remarkably, in the University of Glasgow solution, there is an additional separation line, which may potentially lead to a tertiary vortex too small to be captured in the current grid. Again this situation could be due to the transition treatment meaning a laminar flow in this region. In the EADS solution, the attachment line from the secondary vortex is located very close to the leading edge, indicating that the scheme is more diffusive to capture the secondary vortex. The skin friction contours also demonstrate the effect of the contraction of the wing-fuselage fairing at $x/c \approx 0.25$, showing a break in the high C_f (red) area suggesting a small separated flow region.

Figure 9 shows the spanwise pressure distributions. There is an asymmetry in the DLR (PSP measurement) data indicating that symmetrical flow could not be fully attained during the experiment. Nevertheless, in the range of $\eta < -0.5$ ($\eta > 0.5$) up to the locations around the primary vortices, the data appears to be regular for comparison with the numerical solutions. It should also be noted, however, that the Reynolds number differs for the experimental data and the numerical data (3.5×10^6 versus 5.3×10^6).

All pressure distributions show a vortical flow with primary and secondary vortices. All numerical results agree reasonably well with the experimental data. The NLR and the University of Glasgow solutions show more compact primary vortices (most compact in the University of Glasgow solution) compared to those of EADS and Alenia. More compact vortices are generally more susceptible to vortex breakdown. Indeed, vortex breakdown has occurred in the solutions of NLR and University of Glasgow, as also indicated by the spanwise pressure distributions at $x/c = 0.8$.

Figure 10 presents the total pressure loss contours in the crossflow plane at $x/c = 0.6$ (upstream of vortex breakdown). The primary vortices of the University of Glasgow and the NLR solutions are comparable in compactness, while these are rather smeared in the EADS solution. Again, the University of Glasgow solution shows more distinct secondary vortices compared to the other solutions (the secondary vortices in the University of Glasgow solution are more laminar yielding a larger secondary vortex). The shear layers emanating from the sharp leading edge in the NLR and the EADS solutions appear to have a higher spreading-rate than those in the University of Glasgow solution. All solutions show a similar flow structure in the region where the shear layers, the primary vortex, and the secondary vortex interact.

Figure 11 shows the turbulence Reynolds number (μ_t/μ), defined as the ratio of the eddy viscosity and the molecular dynamic viscosity, in crossflow planes at $x/c = 0.6$ and 0.8. It should be noted that, in order to be able to contrast the turbulence structures, each plot has a different set of contour levels which is determined individually for each plane based on the maximum value occuring within the vortex system. Large variations in the turbulence intensity are indicated.

At $x/c = 0.6$, the University of Glasgow solution shows quite a low turbulence, with highest turbulence occurring inside the boundary layer over the fuselage and not inside the vortex. This low level of turbulence is attributable to the lack of turbulence being generated around the leading edge of the wing. The primary vortex and the secondary vortex themselves, and the shear layers emanating from the leading edge, do not seem to imply any significant turbulence due to the transition treatment. Downstream of vortex breakdown at $x/c = 0.8$, the turbulence level inside the vortex has increased drastically. At $x/c = 0.6$, the NLR solution shows a laminar primary vortex core. At $x/c = 0.8$, downstream of vortex breakdown, large turbulence intensities are introduced into the region near the vortex core. Further downstream, the turbulence is convected away from the core, while at the same time there is a relaminarization of the vortex core. In the EADS solution (with vortex breakdown absent), the turbulence shows to be concentrated inside the vortex core.

In contrast to the case of Euler computations (Refs. 8, 9) where it would suffice to focus on

the aspects of numerical dissipations, one should also consider the differences in the turbulence modelling in trying to explain the differences in the solutions obtained by the various RANS methods. In this respect, assuming that the k-ω turbulence models used are basically equivalent, the production limiters and the transition treatment may be considered as the most important factors.

Both the EADS and the NLR methods employ central schemes with Jameson's type of artificial dissipation. Assuming these methods have comparable numerical dissipations, the more smeared vortices in the EADS solution may be attributed to the uniform limiter (of the production term in the k equation) which is insensitive to vortical flow structure. Although the overall turbulence Reynolds number is significantly lower than that of the NLR solution, the limiter implies concentration of the high values of the turbulence Reynolds number in the vortex core region, inhibiting the formation of a compact vortex.

In both the University of Glasgow and the NLR methods, where the same type of sensor r is used to detect vortex cores, the two different approaches employed to control the turbulence production lead to two completely different mechanisms in capturing the structure inside the vortex. The NLR approach results in some details that resolve a laminar vortex core. The other approach, employed in the University of Glasgow method, does not seem to be sensitive in locations upstream of the vortex breakdown. Here, the compact vortices should therefore be associated more with Osher's upwind scheme (applied to the convective terms), which is known to have less numerical dissipations than the central schemes.

4.2 Case 2: roll-motion about body axis

In this case, the delta wing is making a roll-motion around the body axis with a maximum angle of attack of 17^o. The rolling motion is counterclockwise from pilot view. In this motion, the angle of attack and the side-slip angle are changing periodically with a phase difference of 90^o. The angle of attack reaches its maximum value $\alpha_0 = 17^o$ at $\phi = 0^o$ when the body axis coincides the inertial (earth-fixed) axis. This position corresponds to zero side-slip angle. When $\phi = 90^o$ the side-slip angle reaches its maximum value of 17^o when the angle of attack is zero. For $\phi > 90^o$, the lower surface becomes the leeward side, and therefore vortices should be expected on the lower surface. The position of $\phi = 180^o$ is opposite to that of $\phi = 0^o$. At $\phi = 0^o$ ($\phi = 180^o$), the upper surface is the leeward (windward) side and the lower surface is the windward (leeward) side. The solutions presented are obtained during the third cycle of the roll-motion.

Figures 12 and 13 show the upper and lower surface pressure at roll angle $\phi = 30^o$. The axis shown is the earth-fixed axis coinciding with the body axis at $\phi = 0^o$, indicating the view angle used for the presentation. The results from Alenia (Figure 13) are obtained using a grid coarsened

by taking every other point in both the chordwise and spanwise directions. The contour levels are the same as those in Figure 12. All solutions produce the same asymmetric effect of the roll-motion. The lower surfaces have quite similar patterns. On the upper surface, stronger vortices are evident on the port side. The EADS and Alenia solutions appear to be on a margin of a vortex breakdown on the port side. In the NLR solution, vortex breakdown has occurred on the port side and, further downstream, on the starboard side. The University of Glasgow solution shows a vortex breakdown well upstream at $x/c \approx 0.5$ on the port side, but the starboard side shows only a marginal vortex breakdown. All solutions capture the secondary vortices.

Figure 14 presents the total pressure loss contours on the crossflow plane at $x/c = 0.8$ and $\phi = 30^o$. The streamwise direction is out of the paper. The port side is on the left side of the picture. In the University of Glasgow solution, $x/c = 0.8$ corresponds to a plane downstream of the vortex breakdown location, where there is a large region of significant total pressure loss. In the NLR solution, this location is just upstream of vortex breakdown, and the vortex structure similar to that of the EADS solution is largely maintained.

Figure 15 shows the total pressure loss contours at $x/c = 0.8$ and $\phi = 90^o$. The streamwise direction is out of the paper. The port side is on the left side of the picture. There is no indication of vortices, and all solutions show clearly the effect of the side-slip with flow separation on the leeward side of the fuselage. The EADS and the NLR results are quite similar. The University of Glasgow solution shows an asymmetry in the flow separation (with respect to the horizontal symmetry plane).

Figure 16 shows the variation of the lift and drag coefficients during the third cycle. The force and moment coefficients result from integration over the wing surface (excluding the sting surface). In the EADS result, however, the skin-friction is not included in the integration. A close agreement in the lift coefficient is demonstrated, with small deviations near the roll-angles $\phi = 0^o$ and $\phi = 180^o$ where the angle of attack reaches the extreme values. The variation of lift is nearly in phase with the roll-motion. A good agreement is also shown in the drag coefficient, except that at $\phi = 90^o$ the NLR solution gives a considerably higher drag than that of the EADS solution. It should be recalled that the skin-friction is not included in the surface integration of the EADS solution. At this roll-angle, vortices do not appear in the flow field, such that the difference can also be attributed to the difference in the momentum loss inside the boundary layer and the separated flow over the fuselage.

In Figure 17, all solutions show an overall good agreement in the pitch-moment and roll-moment coefficients. The absolute maximum value of the pitching moment is highest in the NLR solution.

This maximum value occurs near $\phi = 0^o$ and $\phi = 180^o$ where the angle of attack reaches its extreme values. Near these conditions, the NLR solution contains vortex breakdown, shifting the center of pressure towards the front part and thus increasing the pitching moment.

A cosine type of harmonic analysis has been performed for the spanwise pressure coefficient distributions at $x/c = 0.8$. The fundamental harmonic (Figure 18) demonstrates a good agreement showing the presence of the leading edge vortices and the effect of the fuselage. It should be recalled that the Alenia solution is obtained using a coarser grid, resulting in lower and smeared pressure peaks near the leading edge vortices. All solutions produce quite the same results for the first harmonic (Figure 19). The first harmonic is most dominant for the leading edge vortices, as indicated by the two peaks. The phase difference of about 180^o between the lower and the upper surface is due to the fact that at $\phi = 0^o$ ($\phi = 180^o$) the upper (lower) surface is the leeward side on which the vortices occur. A close agreement is also shown for the second harmonic (Figure 20). It shows pronounced fuselage effects at the maximum side-slip at roll-angles $\phi = 90^o$ and $\phi = 270^o$.

4.3 Case 3: roll-motion about wind axis

In this case, the delta wing WI1-SLE is making a roll-motion around the wind axis at $\alpha = 10^o$. The rolling motion is counterclockwise from pilot view. The center of rotation is on the centerline at $x/c = 0.5625$ dividing the delta wing into a front part ($x/c < 0.5625$) and an aft part. The roll-motion induces cross-flow on the wing surface, on the front part in the positive y-direction (towards the starboard side), and on the aft part in the negative y-direction (towards the port side).

The same CO-topology is used for the computational grids as that illustrated in Figure 6. The grid dimension is $144 \times 288 \times 80$ giving a total number of grid cells of $3,317,760$.

Figure 21 presents the spanwise distributions at chordwise positions $x/c = 0.6$ and 0.8. The effect of the roll-motion can be seen as higher suction peaks in the vortex cores on the port side. All numerical results show a similar vortex structure with primary and secondary vortices. The University of Glasgow solution, like in the previous cases, shows distinct suction peaks of the secondary vortices, which may be due to more laminar vortices. The NLR and the University of Glasgow solutions give on the port side a suction level of the secondary vortices in almost the same locations, while larger discrepancies are shown on the starboard side. The EADS solution shows more outboard location of the secondary vortices with lower suction levels.

A close agreement on the pressure contours on the upper surface are shown in Figure 22. There is no indication of vortex breakdown. A region with a minimum pressure on the center of the wing corresponds with the location of the maximum thickness. It can be observed that the flow

asymmetry on the front part has an asymmetry opposite to that on the aft part. In the region bounded by the trailing edge and the cropped wing tip, the crossflow due to the roll-motion seems to have a more pronounced effect in the University of Glasgow solution than in the other solutions.

5 Conclusions

Numerical and experimental investigations of leading edge vortices around delta wing configurations in transonic flows have been addressed. Two geometries of delta wing have been considered: (i) the PSP wing/sting model for steady calculations and unsteady calculations of a roll-motion around the body axis, and (ii) the WI1-SLE model of an isolated delta wing for unsteady calculations of a roll-motion around the wind axis. Comparisons with experimental data and code-to-code comparisons of the computational results have been presented.

Recalling the results obtained previously using the Euler methods (Ref. 9) , clearly the RANS methods have shown to be able to produce much closer agreement with the experimental data. Not only that the secondary vortices have been resolved by the RANS methods (which are absent in the Euler solutions due to the lack of viscous effects), much better prediction of the suction peak level and location of the vortex core have also been demonstrated. Detailed code-to-code comparisons indicate that the RANS methods applied are able to produce numerical results that are consistent with the flow physics expected from the roll-motions.

Significant discrepancies are still present, which are mainly due to whether or not vortex breakdown occurs in the solution and, when it occurs, its location which determines the overall flow characteristics of the solution. The results stress the importance of turbulence modelling. It has been shown that different variants of the two-equation k-ω turbulence model can lead to large variations in the turbulence structure of the vortical flow. This articulates the importance of research on turbulence modelling especially for flows with vortex breakdown.

The research performed dealt with forced motions. The next step towards enabling dynamic time-accurate simulations is the simulation of a delta wing in free motions, where the flow solver is coupled with a flight mechanic model. As the aircraft degrees-of-freedom are in general coupled, and the degree of coupling depends on the nature of the manoeuvre and flight conditions, the feasibility of dynamic simulations with one-, three-, and the realistic six-degrees-of-freedom should be assessed in future research. In turn, the dynamic simulations will enable an accurate assessment of the stability and control properties of military air vehicles in relation with affordability considerations such as safety of flight and air combat capability.

6 Acknowledgment

The collaborative research is performed under the auspices of the Western European Armaments Group (WEAG). The results presented in this paper are obtained from Common Exercise I in the framework of THALES JP12.15, which is defined partly based on the outcome of the preceding Common Exercise V of IEPG TA15.

7 References

1. B.R. Williams, W. Kordulla, M. Borsi, and H.W.M. Hoeijmakers. *Comparison of solution of various Euler solvers and one Navier-Stokes solver for the flow about a sharp-edged cropped delta wing*. AGARD-CP-494, 1994.
2. A. Hilgenstock, W. Kordulla, and A. Meister. *Common Exercise II on the IEPG delta wing WI1-SLE Navier-Stokes and Euler+ solutions on the common Aermacchi C-H-Grid*. DLR-IB 221-93 C 12, 1993.
3. M.T. Arthur. *WEAG TA-15 Common Exercise III on grid adaptation in vortical flow simulations, Part I: Euler solutions*. DRA/AS/ASD/TR96073/1, April 1997.
4. M.T. Arthur. *WEAG TA-15 Common Exercise III on grid adaptation in vortical flow simulations, Part II: Navier-Stokes solutions*. DRA/AS/ASD/SP97550/1.0, December 1997.
5. M.T. Arthur, W. Kordulla, F.J. Brandsma, and N. Ceresola. Grid adaptation in vortical flow simulations. *AIAA Paper 97-2308*, 1997.
6. N. Ceresola. *WEAG-TA15 Common Exercise IV -Time accurate Euler calculations of vortical flow on a delta wing in pitch motion*. Alenia Report 65/RT/TR302/98182, 1998.
7. M.T. Arthur, F.J. Brandsma, N. Ceresola, and W. Kordulla. Time accurate euler calculations of vortical flow on a delta wing in pitching motion. *AIAA Paper 99-3110*, 1999.
8. W. Fritz. *WEAG TA 15 Common Exercise V*. DASA Report Dasa/S/STY/1820, 2000.
9. W. Fritz, M.T. Arthur, F.J. Brandsma, K.-A. Bütefisch, and N. Ceresola. Time accurate euler calculations of vortical flow over a delta wing in rolling motion. RTO/AVT Vortex Flow Symposium, Loen, Norway, 2001.
10. N. Kroll, P. Aumann, W. Bartelheimer, H. Bleecke, B. Eisfeld, J. Lieser, R. Heinrich, M. Kuntz, E. Monsen, J. Raddatz, U. Reisch, and B. Roll. *FLOWer Installation and User Handbook*. DLR Doc.Nr.:MEGAFLOW-1001, 1998.
11. D. C. Wilcox. *Turbulence Modelling for CFD*. DCW Industries, 1998.
12. J.C. Kok. Resolving the dependence on freestream values for the k-ω turbulence model. *AIAA Journal*, 38(7):1292–1294, 2000.
13. J.C. Kok and S.P. Spekreijse. *Efficient and accurate implementation of the k-ω turbulence model in the NLR multi-block Navier-Stokes system*. NLR TP-2000-144 (presented at ECCOMAS 2000, Barcelona, Spain, 11-14 September, 2000), 2000.
14. F.J. Brandsma, J.C. Kok, Dol. H.S., and A. Elsenaar. Leading edge vortex flow computations and comparison with DNW-HST wind tunnel data. RTO/AVT Vortex Flow Symposium, Loen, Norway, 2001.
15. J.W. Boerstoel, A. Kassies, J.C. Kok, and S.P. Spekreijse. *ENFLOW, A full-functionality system of CFD codes for industrial Euler/Navier-Stokes Flow Computations*. NLR TP 96286, 1996.

16. S. Osher and S.R. Chakravarthy. Upwind schemes and boundary conditions with applications to euler equations in general coordinates. *J. Computational Physics*, 50:447–481, 1983.
17. F. Cantariti, L. Dubuc, B. Gribben, M. Woodgate, K.J. Badcock, and B.E. Richards. *Approximate Jacobians for the solution of the Euler and Navier-Stokes equations*. Glasgow University Aero report 5, 1997.
18. F. Cantariti, M. Woodgate, K. Badcock, and B. Richards. *Solution of the Navier-Stokes Equations in Three dimensions using a fully unfactored method.* Glasgow University Aero report 9908, 1999.
19. A. Jameson. Time dependent calculations using multigrid with application to unsteady flows past airfoils and wing. *AIAA Paper 91-1596*, 1991.
20. K.J. Badcock, F. Cantariti, L. Dubuc, and B.E. Richards. Simulation of unsteady turbulent flows around moving aerofoils using the pseudo time method. *Int. J. Num. Meth. Fluids*, 32:584–604, 2000.
21. V. Selmin. The node-centred finite volume approach: bridge between finite difference and finite elements. *Comp. Meth. Appl. Mech. Eng.*, 102:107–138, 1993.
22. R.H. Engler and Ch. Klein. First results using the new DLR PSP system - intensity of lifetime measurements. Wind Tunnels and Wind Tunnel Test Techniques, 14-16 April 1997, Cambridge, UK, 1997.
23. R.H. Engler, Ch. Klein, E. Merlo, and P. van Amerom. 360^o PSP measurements in transonic flow. 19th ICIASF Congress, Cleveland, Ohio, USA, pages 149–158, 2001.
24. R. Engler, S. Fonov, C. Klein, K-A. Bütefisch, D. Weiskat, K-W. Bock, and W. Fritz. Study of unsteady behaviour of a rotating 65^o delta wing at $M = 0.8$ using pressure sensitive paint (PSP). RTO/AVT Vortex Flow Symposium, Loen, Norway, 2001.

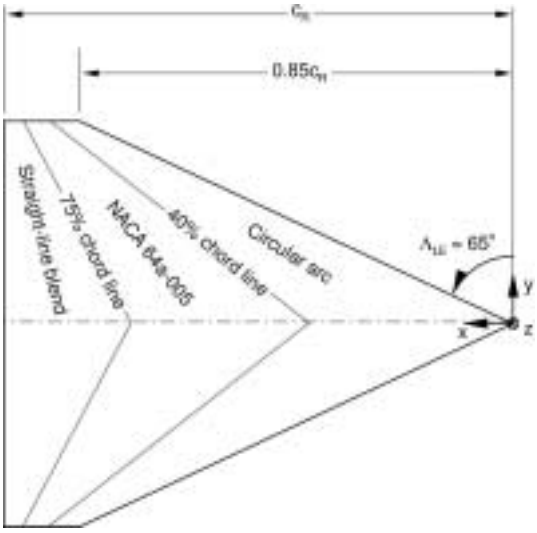

Fig. 1 Planform of the delta wing.

Fig. 2 Roll-motion about the body axis.

Fig. 3 Roll-motion about the wind axis.

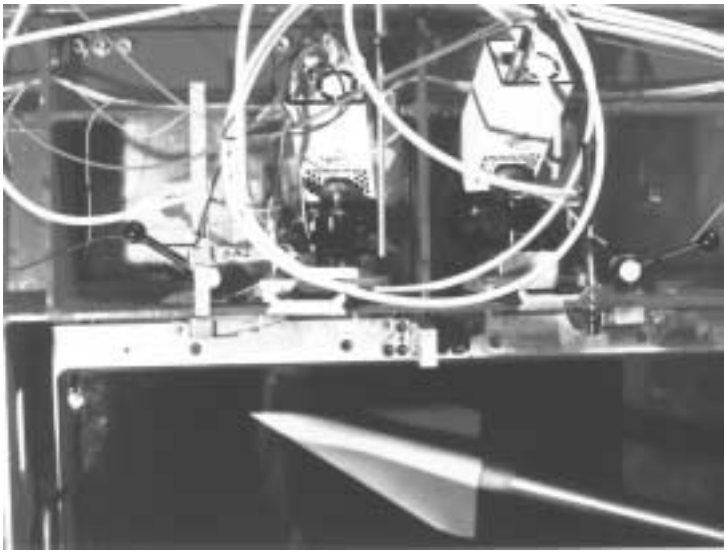

Fig. 4 View of test section wall with PSP cameras

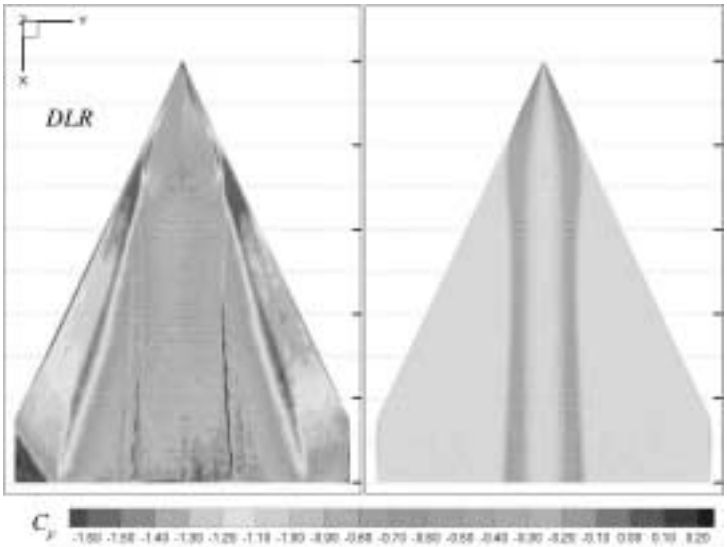

Fig. 5 Case 1: experimental upper surface C_p ($\mathrm{Re} = 3.5 \times 10^6$).

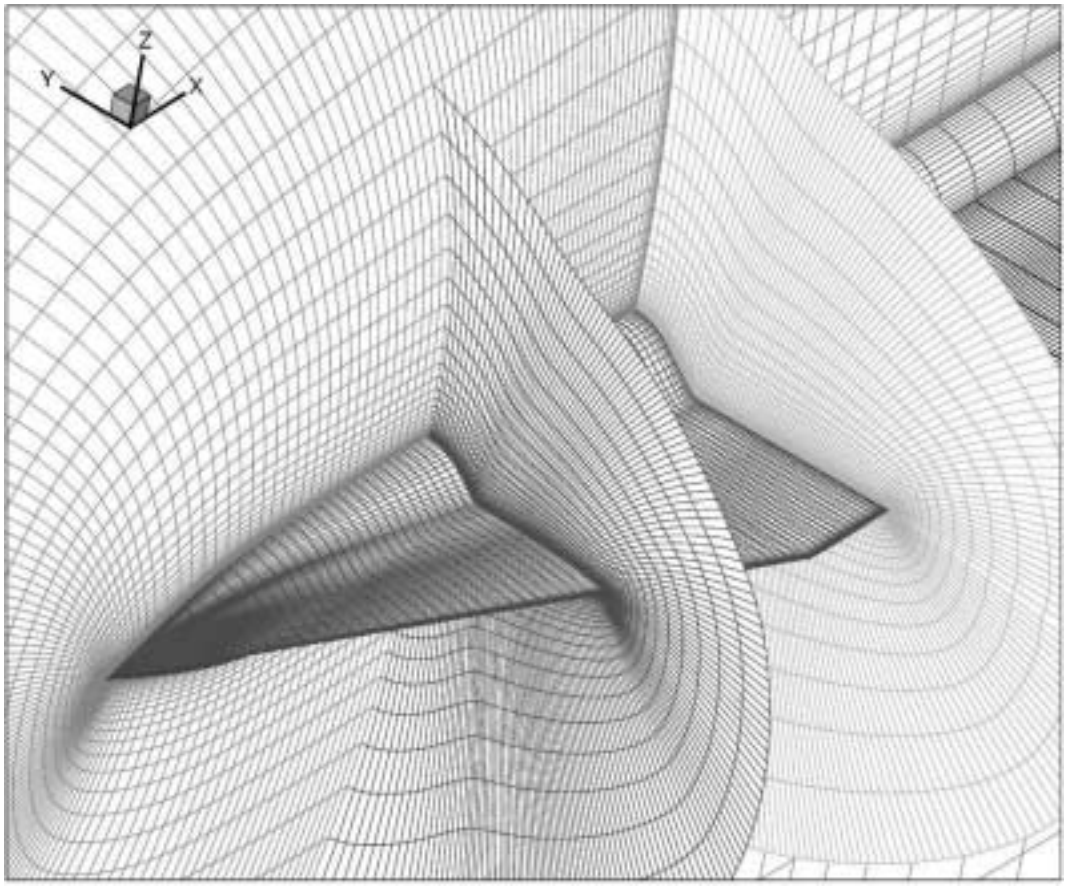

Fig. 6 Computational grid of the PSP model used for Case 1 and Case 2.

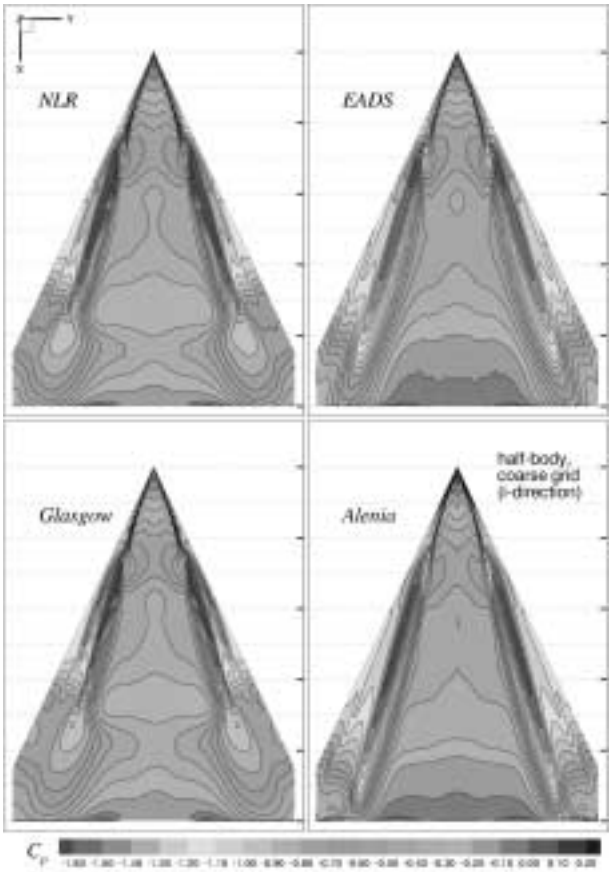

Fig. 7 Case 1: numerical upper surface C_p contours ($\mathrm{Re} = 5.3 \times 10^6$*).*

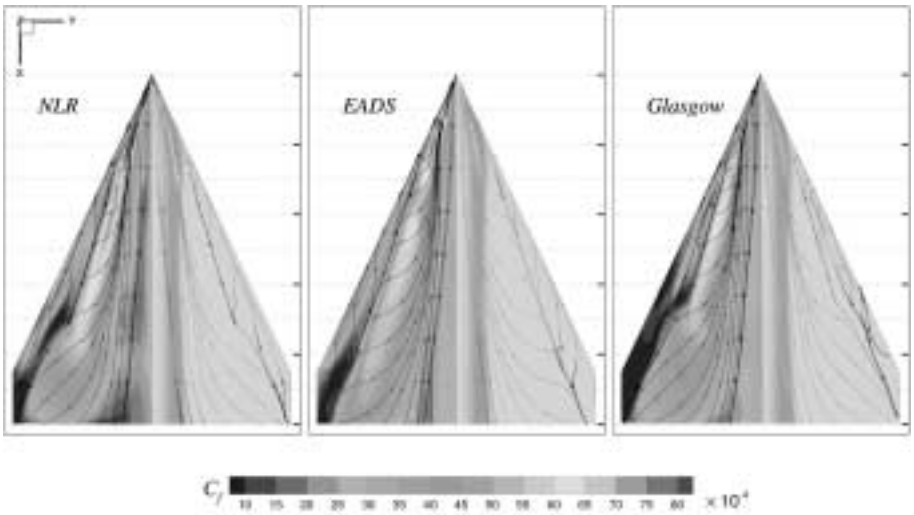

Fig. 8 Case 1: C_f contours and limiting streamlines.

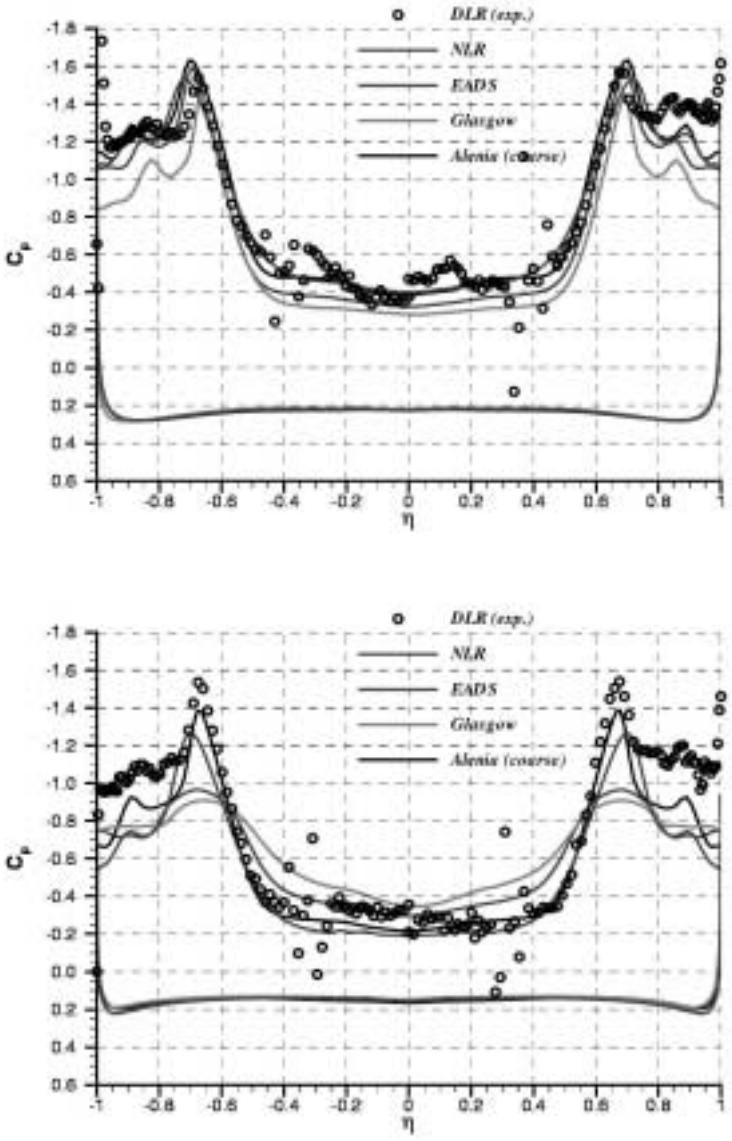

Fig. 9 Case 1: spanwise C_p distributions at $x/c = 0.6$ (upper), and 0.8 (lower). ($\mathrm{Re} = 3.5 \times 10^6$ in experiment, $\mathrm{Re} = 5.3 \times 10^6$ in computations)

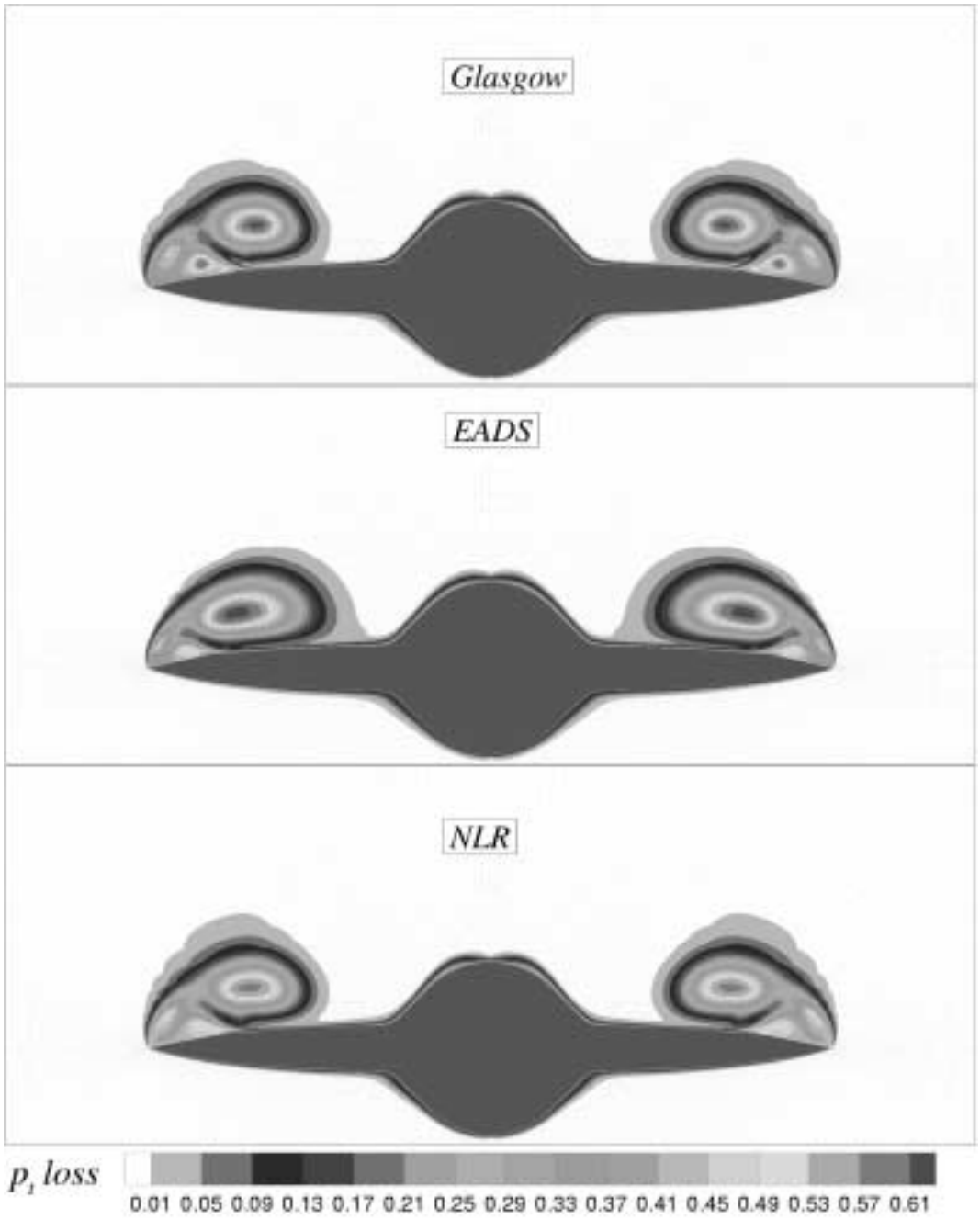

Fig. 10 Case 1: total pressure loss at $x/c = 0.6$.

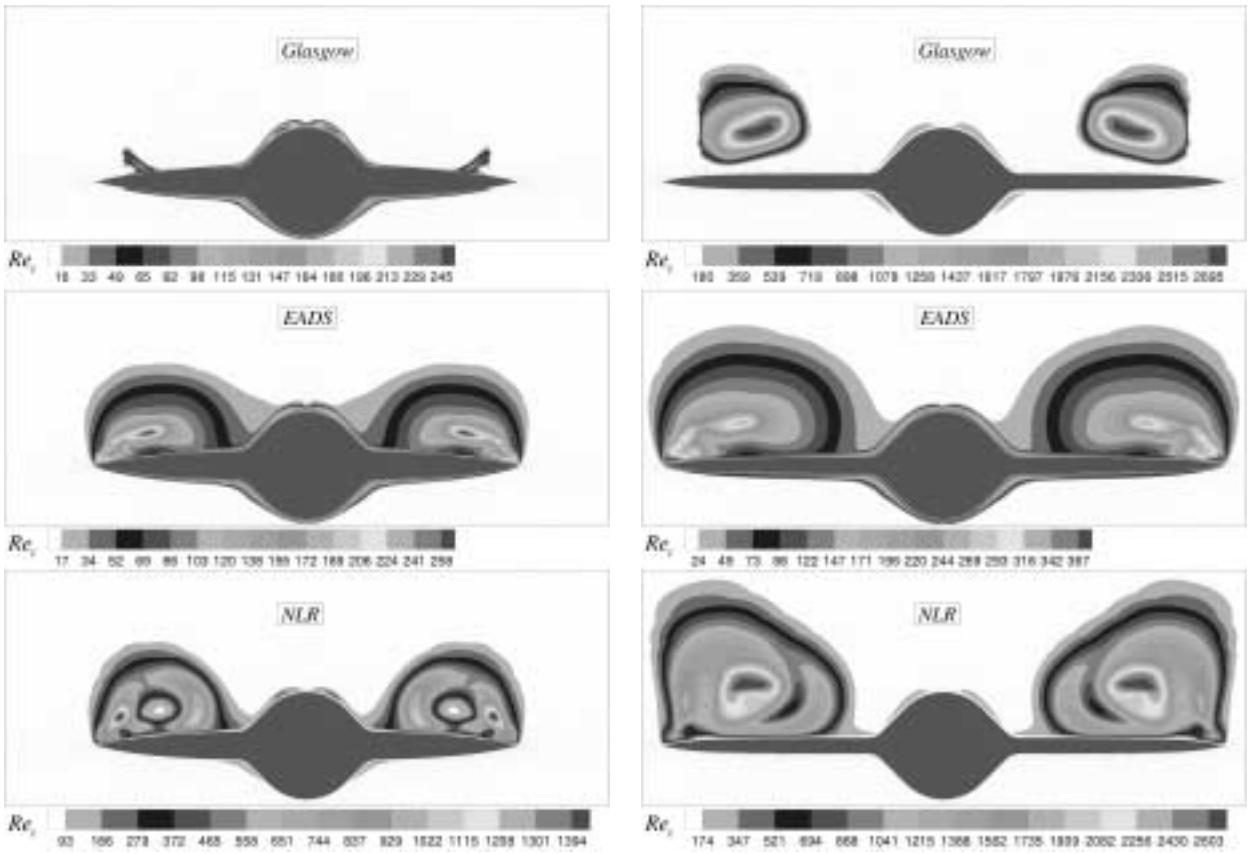

Fig. 11 Case 1: turbulence Reynolds number μ_t/μ at $x/c = 0.6$ and $x/c = 0.8$.

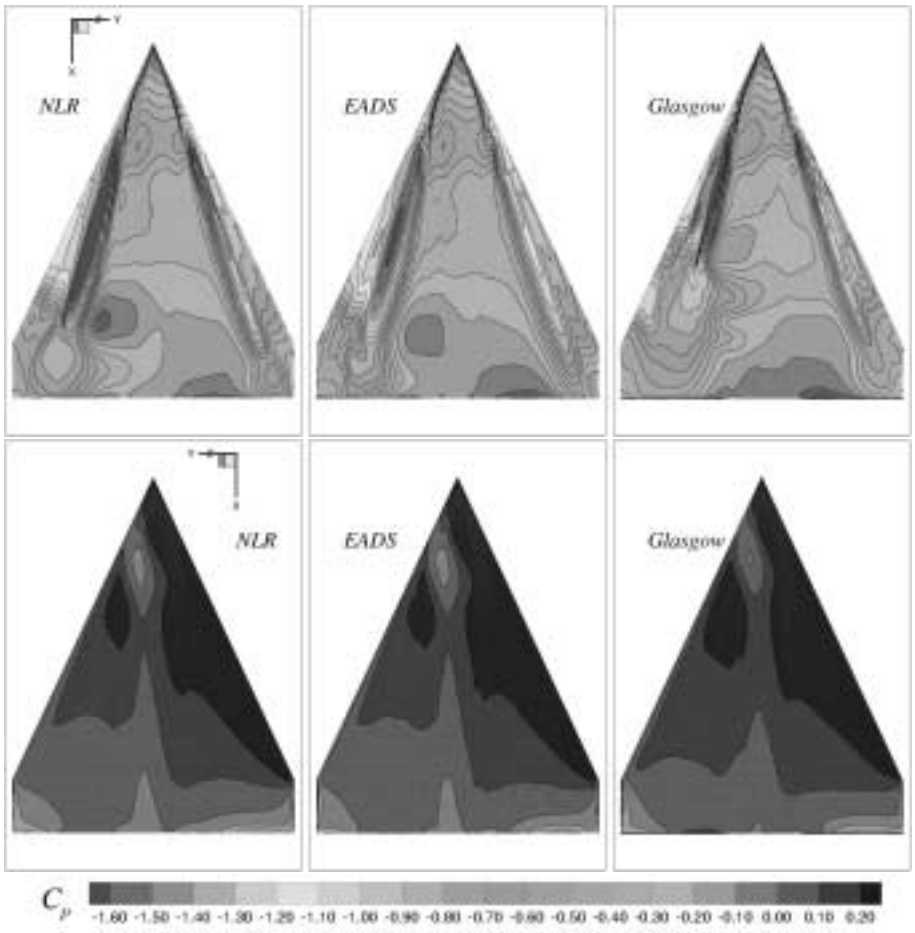

Fig. 12 Case 2: upper and lower surface C_p at $\phi = 30^o$.

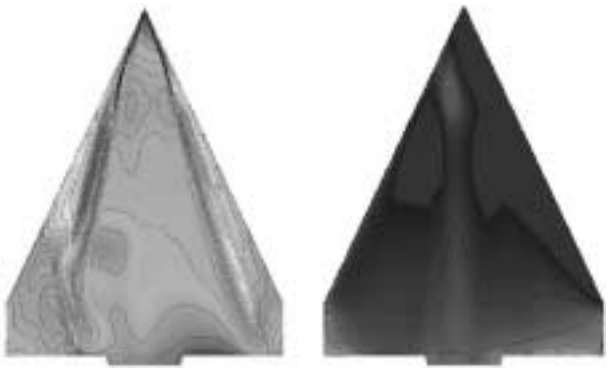

Fig. 13 Case 2: Alenia surface C_p contours at $\phi = 30^o$.

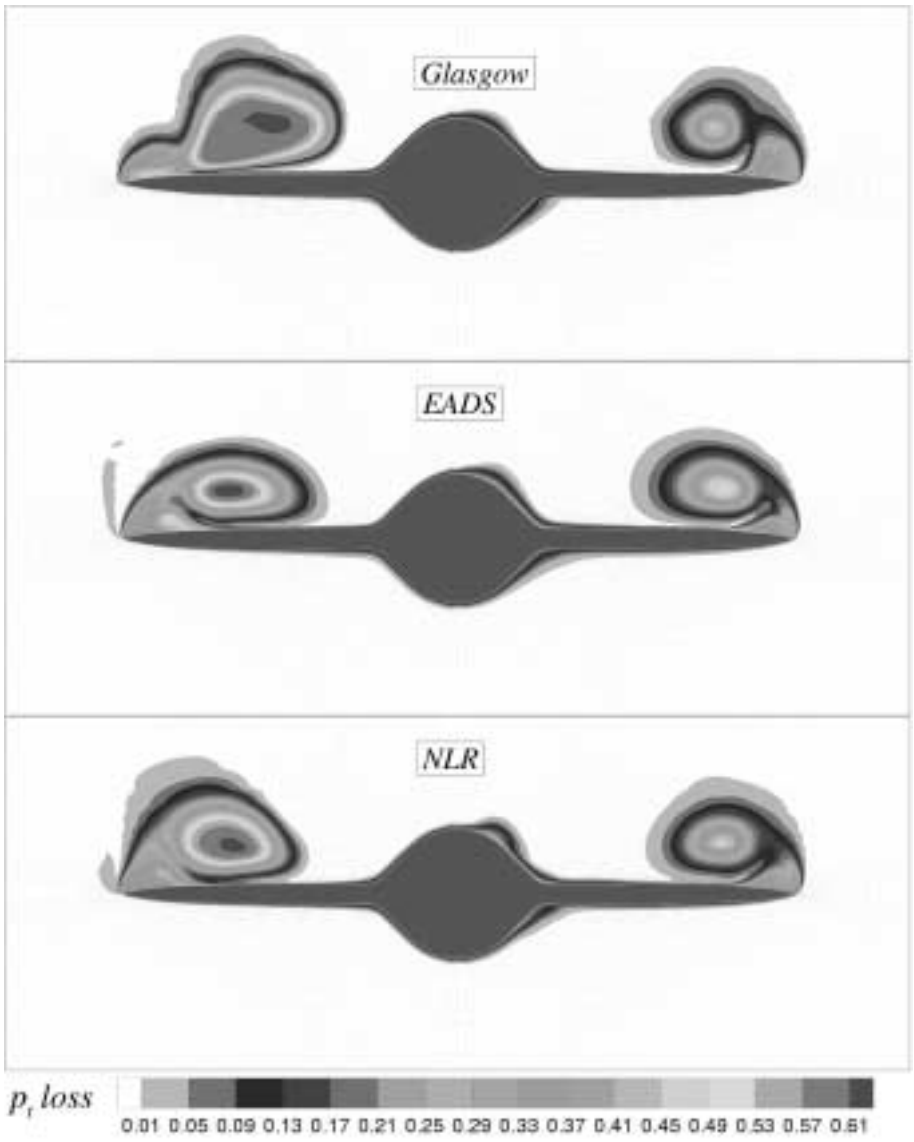

Fig. 14 Case 2: total pressure loss at $\phi = 30^o$, $x/c = 0.8$.

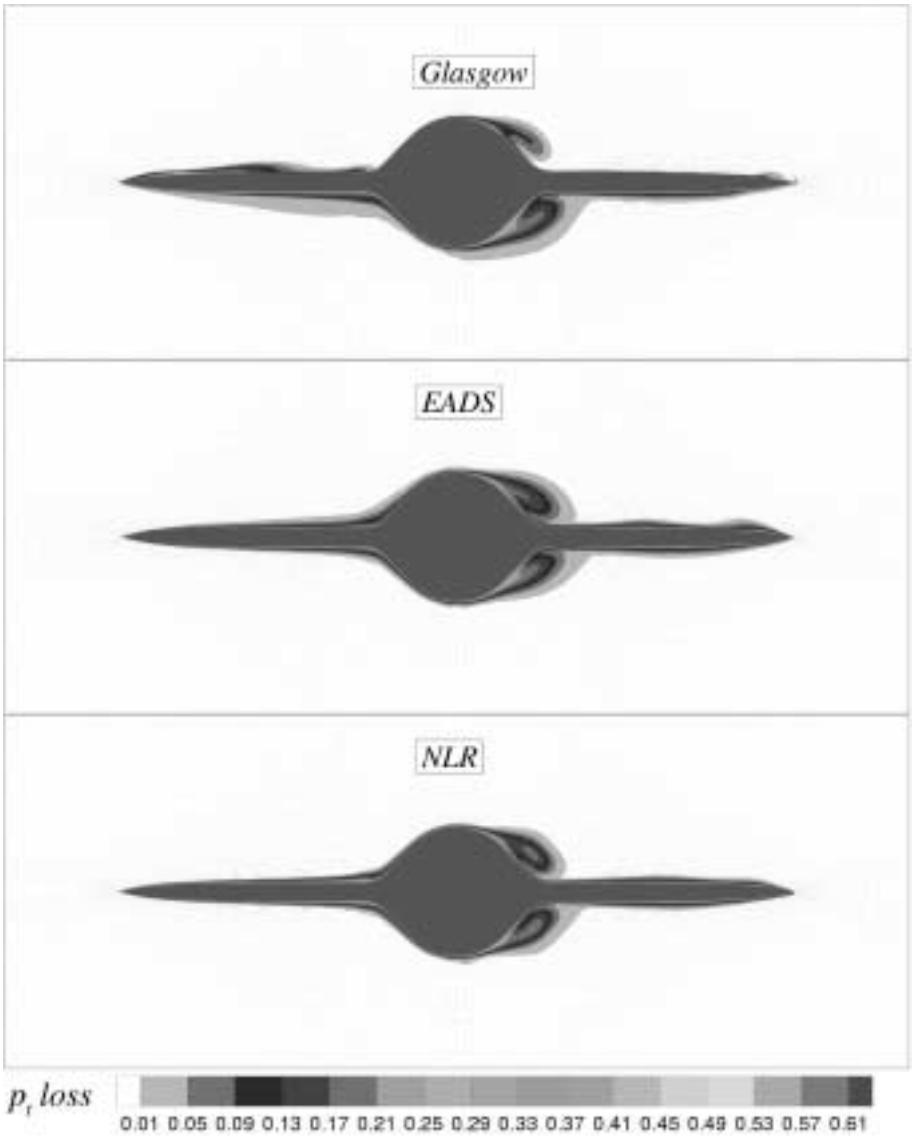

Fig. 15 Case 2: total pressure loss at $\phi = 90^o$, $x/c = 0.8$.

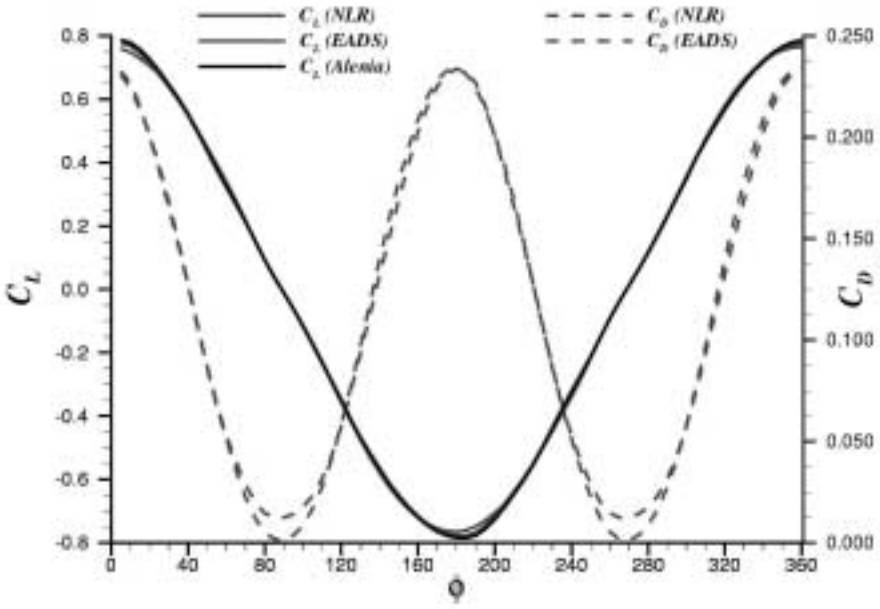

Fig. 16 Case 2: variations of force coefficients.

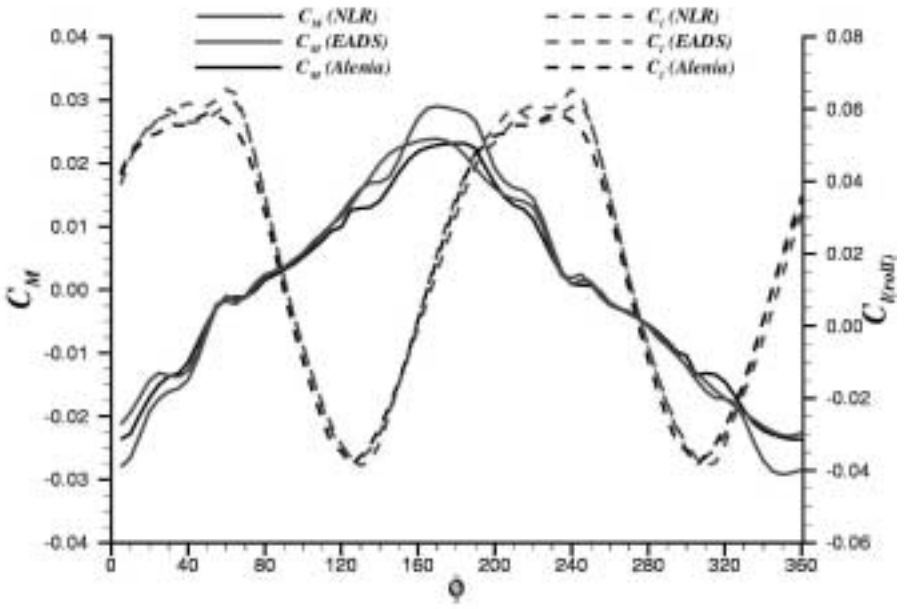

Fig. 17 Case 2: variations of moment coefficients.

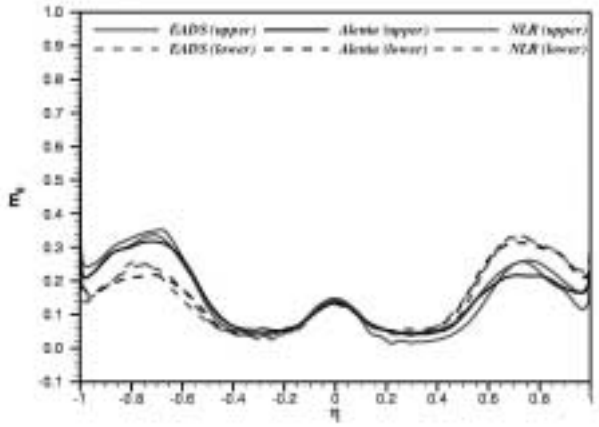

Fig. 18 Case 2: fundamental harmonics at $x/c = 0.8$.

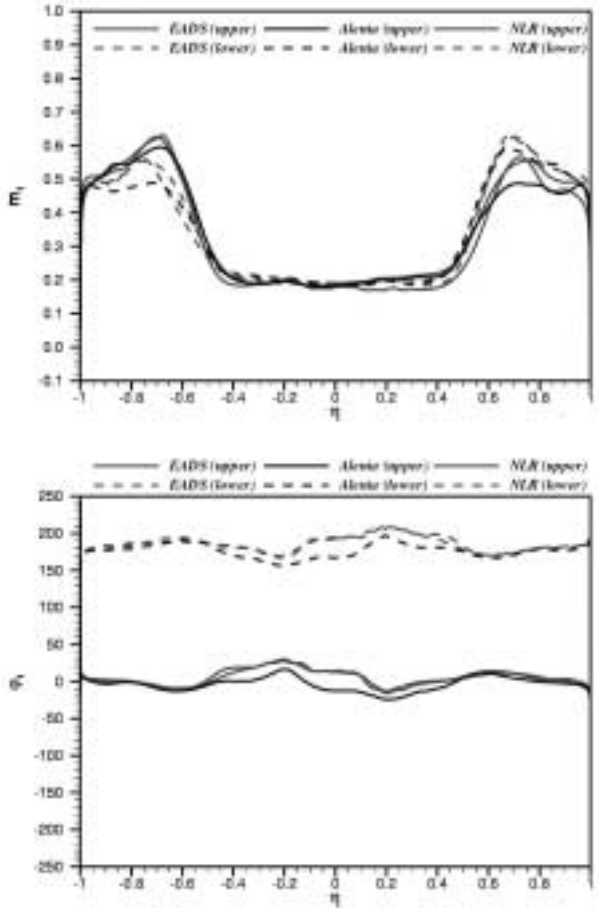

Fig. 19 Case 2: magnitude and phase of 1st harmonic.

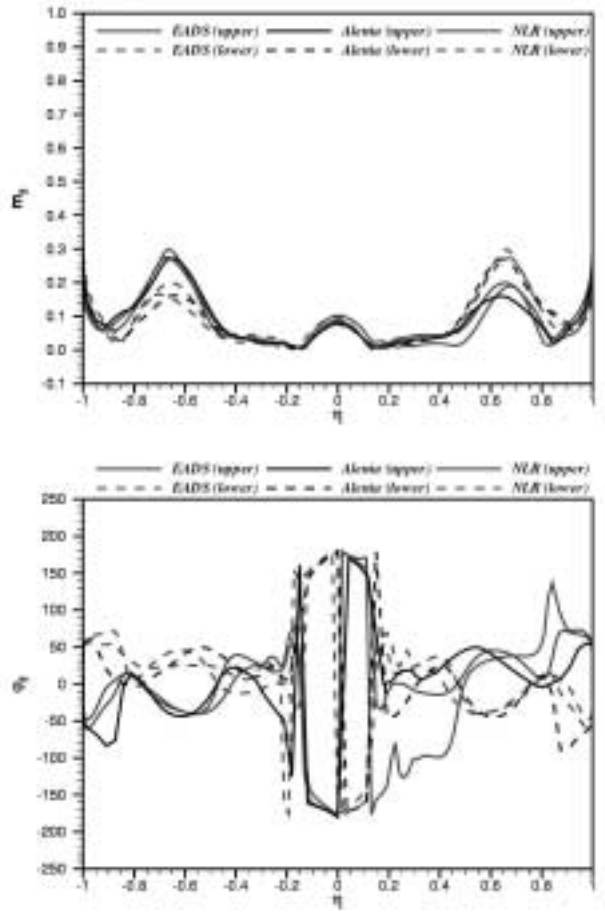

Fig. 20 Case 2: magnitude and phase of 2nd harmonic.

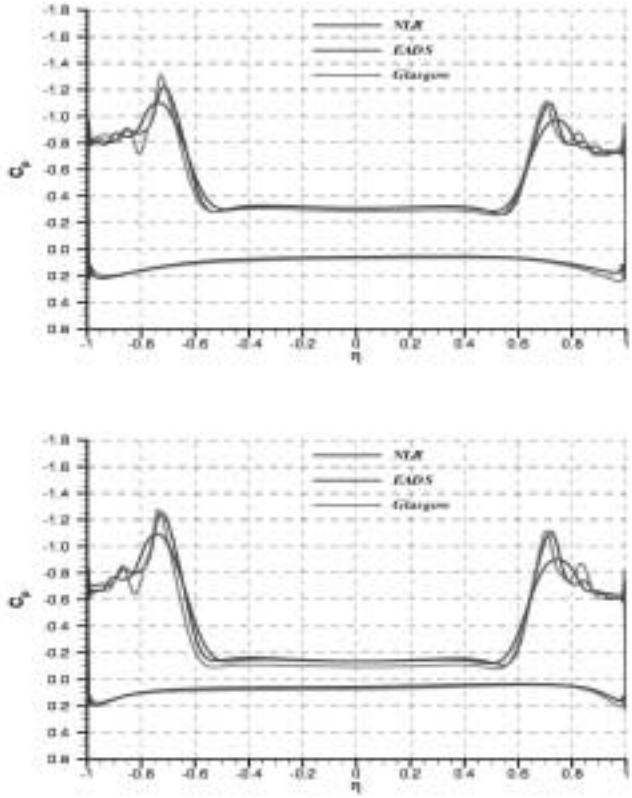

Fig. 21 Case 3: spanwise C_p distributions at 0.6 (upper) and 0.8 (lower).

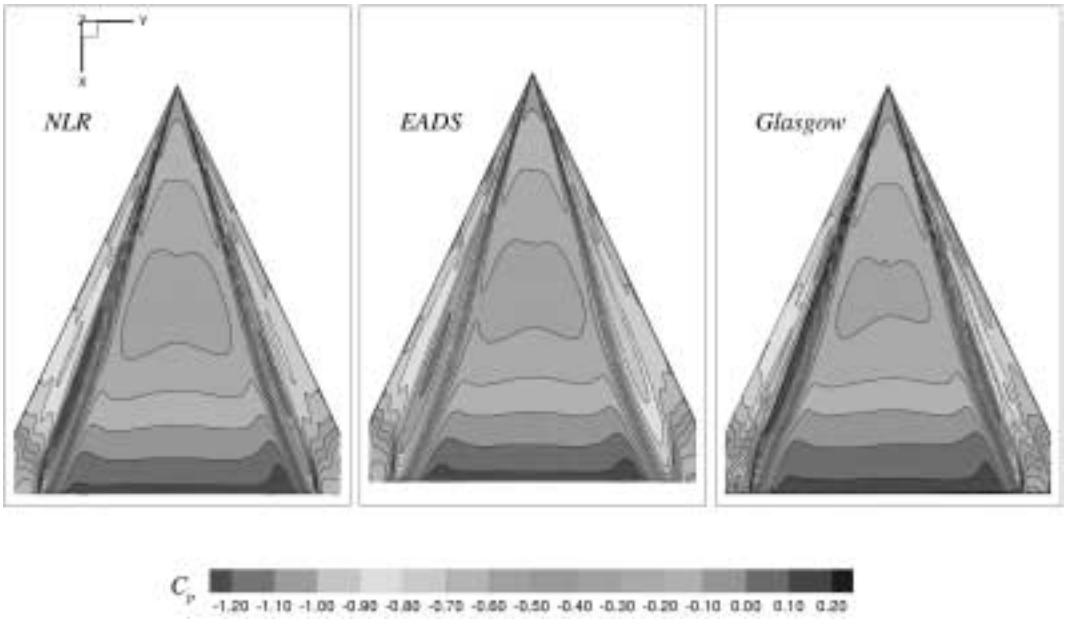

Fig. 22 Case 3: upper surface C_p contours.